

Osiris: A Systolic Approach to Accelerating Fully Homomorphic Encryption

Austin Ebel
New York University
Brooklyn, NY, USA
abe5240@nyu.edu

Brandon Reagen
New York University
Brooklyn, NY, USA
bjr5@nyu.edu

Abstract—In this paper we show how fully homomorphic encryption (FHE) can be accelerated using a systolic architecture. We begin by analyzing FHE algorithms and then develop systolic or systolic-esque units for each major kernel. Connecting units is challenging due to the different data access and computational patterns of the kernels. We overcome this by proposing a new data tiling technique that we name limb interleaving. Limb interleaving creates a common data input/output pattern across all kernels that allows the entire architecture, named Osiris, to operate in lockstep. Osiris is capable of processing key-switches, bootstrapping, and full neural network inferences with high utilization across a range of FHE parameters. To achieve high performance, we propose a new giant-step centric (GSC) dataflow that efficiently maps state-of-the-art FHE matrix-vector product algorithms onto Osiris by optimizing for reuse and parallelism. Our evaluation of Osiris shows it outperforms the prior state-of-the-art accelerator on all standard benchmarks.

I. INTRODUCTION

The ubiquity of cloud computing and online services has caused wide-scale data outsourcing, raising privacy and security concerns. This has sparked an increased interest in techniques for privacy-preserving and confidential computing. These techniques enable evaluating functions directly on encrypted data, ensuring it is always secured while off device. One popular technique for cryptographic confidential computing is fully homomorphic encryption (FHE). FHE provides secure outsourced computation using emerging encryption schemes, making it a natural fit for today’s cloud model. While promising, broad deployment of FHE remains limited due to the significant performance overhead it introduces.

Prior work has made significant progress in addressing these overheads spanning multiple domains. Cryptographers have devised new FHE schemes and optimizations for better performance (e.g., SIMD ciphertext packing [57], hoisting [10], [28], and CKKS’s native fixed-point support [15]). Compiler research has assuaged many of FHE’s programming complexities while simultaneously improving performance, including instruction scheduling [18], [44], [61], SIMD ciphertext packing and data layout [6], [23], [35], [41], and bootstrap placement [2], [9]. Finally, work on hardware acceleration has proposed architectures that provide the computational power needed to overcome the slowdown. These designs span the architectural landscape. Early solutions targeted fixed-function designs to demonstrate the magnitudes of slowdown could be overcome [52], [53]. Others proposed vector architectures, a

natural fit as the core data structure in FHE (polynomial rings) readily maps to the ISAs [25], [54], [58]. Recent efforts have included tiled/clustered architectures and FPGAs. In tiled solutions, processing lanes and NoCs can be reformed to execute different FHE kernels [37], [38], [40]. FPGA specific designs provide immediate speedup running on existing commercially available hardware [3]–[5], [53], [56]. The insights and reported speedup of prior work is substantial. However, there is still room for improvement. For example, fixed-function ASICs do not provide the flexibility to support a variety of FHE workloads nor algorithms; vectors are flexible but rely on complex circuitry for generality and performance (e.g., register files and chaining); tiled/clustered may be difficult to program and require large NoCs.

Systolic architectures can address many of the problems noted above. The rigid, lockstep execution model of a systolic design eliminates the need for data sharing via register files (or chaining), NoC wiring, and promotes minimal control overhead. At the same time, flexibility in data layout and staging provides the necessary generality to support a range of FHE parameters and workloads. In this paper we develop a systolic architecture to accelerate FHE, named Osiris. The main intellectual insight is recognizing and distilling the complexity of FHE into a set of relatively simple computational cells and communication patterns, and the devising a dataflow that enables composing them into a complete architecture that runs in lockstep.

Osiris makes multiple contributions to accomplish this goal. First, we propose and develop individual systolic *units* for each FHE kernel, see Section IV for details. We carefully consider how kernels interact and co-design units with those they connect with to optimize interfaces. Effectively integrating units into a complete systolic architecture is non-trivial. The key challenge is that the number theoretic transform (NTT) kernel naturally works over individual inputs (i.e., limbs). Conversely, the basis conversion (BConv) kernel, which we compute as a matrix multiply, demands limb tiling and interspersing data from distinct limbs to implement as a monolithic 2D systolic array. Naïve solutions would require large buffers between the units to reorganize data and introduce stalls. Our second contribution is to solve this by developing *limb interleaving*.

Limb interleaving tiles unit inputs by interspersing cross sections of distinct limbs for processing, rather than executing each limb entirely one at a time. With limb interleaving, limbs

can then flow directly through the NTT unit and into the BConv unit, eliminating large buffers and stalls. Furthermore, as each unit runs in lockstep, the I/O rates are straightforward to balance. With limb interleaving and the developed systolic units, we comprise a complete systolic architecture capable of accelerating entire FHE workloads, including bootstrapping and neural inference. Osiris further supports recent optimizations to reduce bandwidth including on-the-fly limb extension (OF-Limb), PRNG key generation [3], [54], and twiddle factor decomposition [39].

Efficient hardware is only part of the challenge. Osiris provides high-performance kernel accelerators and efficient interfaces between them, leaving flexibility in how FHE is mapped to it. Optimizing the FHE dataflow is complex and compounded by recent algorithmic advancements to computing matrix-vector products, specifically the baby-step giant-step (BSGS) algorithm [28] and double-hoisting [10]. Both reduce the absolute number of computations in matrix-vector products, and with double-hoisting, the results from computationally demanding kernels are shared and reused, saving work recomputing them. This poses two challenges: masking data movement latency with fewer computations and deciding which data to cache on the chip. Our third contribution is the development of the giant-step centric (GSC) dataflow, which addresses both challenges. In GSC, we schedule kernels such that OF-Limb overlaps with off-chip (baby-step) key reads and size Osiris to balance their latencies. GSC caches partials on chip, exhaustively reusing rotated (baby-step) inputs, see Section V for details. The GSC dataflow combined with our systolic architecture facilitates high performance and eases implementation.

This paper makes the following contributions:

- 1) We analyze FHE kernels, considering data patterns and kernel interaction, to develop a systolic unit for each.
- 2) We propose limb interleaving and show that it enables efficient unit connections (via consistent access patterns) to form a larger systolic architecture, named Osiris,
- 3) We present the GSC dataflow to map state-of-the-art algorithms (BSGS and double hoisted rotations) to Osiris.
- 4) We rigorously evaluate Osiris with standard benchmarks, perform sensitivity studies to understand sources speedup, and conduct roofline analysis to demonstrate the design's balance. Osiris achieves state-of-the-art performance on all benchmarks, with a bootstrap (ResNet-20) speedup of $1.16\times$ ($1.07\times$) over SHARP [37] and average speedup of $6603\times$ over a CPU. We further show near linear performance scaling with increased resources at higher bandwidths, executing ResNet-20 in 23.8 ms at 4 TB/s.

II. BACKGROUND

In this section, we introduce the relevant parameters, notation, and operations of CKKS [15]. An overview of the notation is shown in Table I. When possible, we adopt terminology from prior work [3], [37], [40]. CKKS supports several homomorphic operations on and between plaintext polynomials and ciphertexts, similar to prior HE schemes

TABLE I: CKKS parameter notation and descriptions.

Param.	Description
\mathbf{m}	Message, a vector of real or complex numbers.
$[P]$	Plaintext polynomial encoding the message, \mathbf{m} .
$[[C]]$	Ciphertext encrypting the plaintext polynomial, $[P]$.
N	Power-of-two polynomial ring degree.
n	Length (slots) of the vector message, $n \leq N/2$ (or N).
L	Maximum multiplicative level of $[[C]]$.
ℓ	Current multiplicative level.
Q	Initial polynomial modulus.
q_i	Small moduli in RNS decomposition of $Q = \prod_{i=0}^L q_i$.
α	Limbs in hybrid decomposition basis of Q .
$dnum$	Decomposition number in key-switching, $\lceil (\ell + 1)/\alpha \rceil$.
P	Auxiliary modulus used in key-switching.
p_i	Small moduli in RNS decomposition of $P = \prod_{i=0}^{\alpha-1} p_i$.
L_{boot}	Number of levels consumed by bootstrapping.
L_{eff}	Maximum achievable level after bootstrapping.

such as BGV [11] and BFV [12]. Specifically, we denote the additions (multiplications) of two ciphertexts as HAdd (HMult) and additions (multiplications) of a ciphertext and a plaintext polynomial as PAdd (PMult). We also denote the rotation of a cleartext (ciphertext) by Rot (HRot). To perform these operations, a vector message, \mathbf{m} , is first encoded into a cyclotomic polynomial $[P] = \mathbb{Z}_Q[X]/(X^N + 1)$, with coefficients modulo Q and ring degree N . A ciphertext, $[[C]]$, is a pair of polynomials that can be generated from $[P]$ and is made secure by adding a small amount of random noise to one of the polynomials.

Since Q is often large (on the order of thousands of bits), it is most efficient to decompose a polynomial into many separate polynomials, or *limbs*, each with a smaller size modulus, q_i , such that $Q = \prod_{i=0}^L q_i$, using the Chinese remainder theorem [14]. L sets the ciphertext's maximum *level* and operations such as HMult consume levels. When the current level, ℓ , reaches zero, an expensive Bootstrap procedure is required to increase the ciphertext's level to enable further computation. Bootstrapping consumes a fixed number of levels, L_{boot} , and therefore a ciphertext can only reach an *effective* level, $L_{eff} = L - L_{boot}$ after bootstrapping.

Both HMult and HRot operations transform a ciphertext originally decrypted by a secret key, s , into a ciphertext only decryptable by a new secret key, s' . The most efficient approach to return to s and enable further computation is to multiply the ciphertext with a special *switching* key, swk , to perform a re-encryption of the ciphertext under the secret key, s . However, a naïve multiplication with the swk adds prohibitively large noise. Techniques proposed by Fan and Vercauteren [24] and later by Han and Ki [30] address this issue directly, with a common theme being that they first Decompose a ciphertext into many *digits* and perform this KeyMult operation at a higher modulus. The act of changing a ciphertext's modulus is expensive, requiring many (inverse) number theoretic transforms (I/NTTs) and basis conversion (BConv) operations. In Osiris, we collectively refer to chang-

Algorithm 1: $\text{ModChange}_{\alpha \rightarrow \beta}([A])$

Input: $[A]$, a polynomial of α limbs with modulus Q .

Output: A polynomial with β limbs and modulus Q' .

- 1 $[A_{\text{coeff}}] \leftarrow \text{INTT}([A]_{q_i})_{0 \leq i < \alpha}$
 - 2 $[B_{\text{coeff}}] \leftarrow \text{BConv}_{\alpha \rightarrow \beta}([A_{\text{coeff}}])$
 - 3 **return** $\text{NTT}([B_{\text{coeff}}]_{q'_i})_{0 \leq i < \beta}$
-

ing the RNS representation of a modulus from α limbs to β limbs as ModChange . When $\alpha < \beta$ ($\alpha > \beta$), we refer to the operation as ModUp (ModDown). The Rescale operation is a specific case of ModDown when $\beta = \alpha - 1$. Finally, we adopt the hybrid variant of key-switching [30], similar to existing FHE accelerators [37], [38], [54], and refer readers to prior work [3], [10], [48] for more detail.

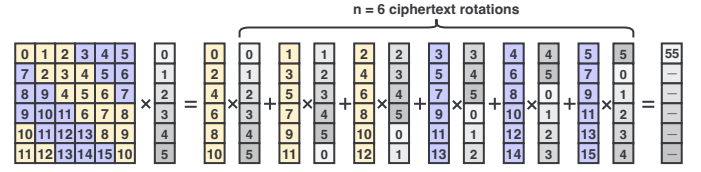
Algorithm 1 describes this ModChange operation. Note that separate I/NTTs must be applied to each limb and that the modulus changes from $Q = \prod_{i=0}^{\alpha-1} q_i$ to $Q' = \prod_{i=0}^{\beta-1} q'_i$. We also emphasize that the core operation in BConv a matrix-matrix multiplication between a *base table* of scaling factors and the input polynomial. In Section IV, we show how to accelerate this matrix multiplication with a 2D systolic array.

III. FHE MATRIX-VECTOR PRODUCTS

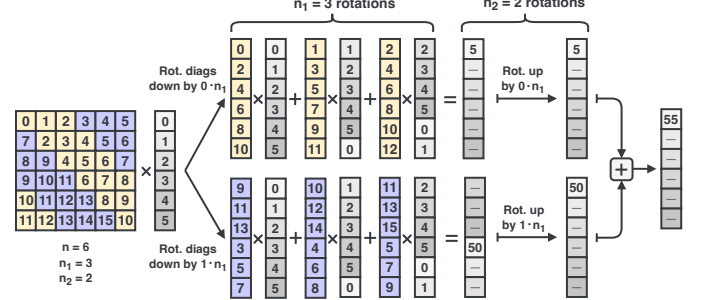
We now introduce how fast FHE matrix-vector products are implemented. We start with the naïve approach and then describe two compounding optimizations: the *baby-step giant-step* (BSGS) algorithm and *hoisting*. To the best of our knowledge, Osiris is the first ASIC to adopt state-of-the-art hoisting techniques [10], [28] for matrix-vector products. Matrix-vector products can account for 70% to 99% of the private inference latency in FHE [23]. Therefore, we tailor specific mapping strategies for this algorithm on Osiris.

Diagonal Method: The simplest approach to FHE matrix-vector products is the diagonal method [27]. Here, one first extracts the *generalized diagonals* of a matrix, \mathbf{M} . That is, diagonals of the form $\text{diag}_k = \mathbf{M}_{[0,k]}, \mathbf{M}_{[1,1+k]}, \dots, \mathbf{M}_{[w-1,w-1+k]}$, where w is the width of the matrix and the second index is taken modulo w . Each diagonal is multiplied with a rotated input ciphertext. Figure 1a shows the approach, where the number of non-zero diagonals, n , is 6. Note that since we have rotated the ciphertext n times, we must perform n distinct key-switch operations, each computing a Decompose , KeyMult , and ModDown , to realign partial products under the same secret key. Thus, the runtime can be seen as $\mathcal{O}(n)$.

Baby-Step Giant-Step: The baby-step giant-step (BSGS) algorithm reduces the runtime complexity of homomorphic matrix-vector products to $\mathcal{O}(\sqrt{n})$ [28]. Therefore, as the number of non-zero diagonals increases, so does the impact of this optimization. We show the BSGS approach in Algorithm 1b and modify the running matrix-vector example from Figure 1a. Here, matrix-vector products are parameterized by two constants: n_1 , the number of baby steps or input rotations, and n_2 the number of giant steps or partial product rotations, where $n_1 n_2 = n$. In Figure 1b, we set $n_1 = 3$ and $n_2 = 2$ such that $n_1 n_2 = 6$. The distinction between n_1 and n_2 lies



(a) The diagonal method. $n = 6$ ciphertext rotations are required, one per non-zero diagonal (including trivial rotation by 0).



(b) Extending the diagonal method with BSGS. Note that only $n_1 + n_2 = 5$ rotations are required and that $n_1 n_2 = n = 6$.

Fig. 1: Visualizing how the BSGS algorithm reduces the number of ciphertext rotations in matrix-vector products.

Algorithm 2: BSGS matrix \times vector algorithm. [28]

Input: ct encrypting vector message, \mathbf{m} , \mathbf{M}_{diag} the diagonals of \mathbf{M} , an $n \times n$ matrix with $n = n_1 n_2$.

Output: $\text{ct}' = \mathbf{M} \times \text{ct}$.

- 1 **for** $i = 1; i < n_1; i = i + 1$ **do**
 - 2 $\text{ct}_i \leftarrow \text{HRot}_i(\text{ct})$
 - 3 $\text{ct}' \leftarrow (0, 0)$
 - 4 **for** $j = 0$ **to** $n_2; j = j + 1$ **do**
 - 5 $\mathbf{r} \leftarrow (0, 0)$
 - 6 **for** $i = 0, i < n_1; i = i + 1$ **do**
 - 7 $\mathbf{r} \leftarrow \text{HAdd}(\mathbf{r}, \text{PMult}(\text{ct}_i, \text{Rot}_{-n_1 \cdot j}(\mathbf{M}_{\text{diag}}^{n_1 \cdot j + i})))$
 - 8 $\text{ct}' \rightarrow \text{HAdd}(\text{ct}', \text{HRot}_{n_1 \cdot j}(\mathbf{r}))$
 - 9 **return** ct'
-

in the magnitude of their rotations and when the rotations are performed. We first generate the n_1 input rotations (baby steps) of the input ciphertext. Each baby-step rotation is then multiplied with n_2 diagonals.

Unlike in the diagonal method, we are left with n_2 partial products, each offset by some multiple of n_1 . Therefore, $n_2 - 1$ non-trivial partial product rotations (giant steps) are required to realign ciphertexts before the final reduction. Rotations are expensive, and the key insight of BSGS is that we can choose to reuse ciphertext rotations and *instead* rotate matrix diagonals (Line 7, Algorithm 2). Since matrix diagonals are known a priori (weights in convolutions or constant matrices in bootstrapping), they can be trivially rotated before being encoded. This observation reduces the number of ciphertext rotations to just $n_1 + n_2$, and rotations are minimized when $n_1 = n_2 = \sqrt{n}$.

Hoisting: Hoisting is a cryptographic optimization that further reduces the complexity of matrix-vector products. This tech-

Limb 3	0 ₁₂	1 ₁₃	2 ₁₄	3 ₁₅	4 ₁₂	5 ₁₃	6 ₁₄	7 ₁₅	8 ₁₂	9 ₁₃	10 ₁₄	11 ₁₅	12 ₁₂	13 ₁₃	14 ₁₄	15 ₁₅
Limb 2	0 ₈	1 ₉	2 ₁₀	3 ₁₁	4 ₈	5 ₉	6 ₁₀	7 ₁₁	8 ₈	9 ₉	10 ₁₀	11 ₁₁	12 ₈	13 ₉	14 ₁₀	15 ₁₁
Limb 1	0 ₄	1 ₅	2 ₆	3 ₇	4 ₄	5 ₅	6 ₆	7 ₇	8 ₄	9 ₅	10 ₆	11 ₇	12 ₄	13 ₅	14 ₆	15 ₇
Limb 0	0 ₀	1 ₁	2 ₂	3 ₃	4 ₀	5 ₁	6 ₂	7 ₃	8 ₀	9 ₁	10 ₂	11 ₃	12 ₀	13 ₁	14 ₂	15 ₃

limb coefficient index_{input/output order}

Fig. 2: Matrix representation of a polynomial ($N = 16$, $\ell = 3$) in natural order. Element i_o indicates that the coefficient at index i within its limb is in the o 'th set of coefficients to be processed by a hardware unit.

nique can be applied to stages of the BSGS algorithm that share a common result. For example, rotations to the *same* input ciphertext share a common Decompose output. Therefore, we can perform this computation only once, *hoisting* it out and reusing its result for all n_1 baby-step rotations. We further discuss the state-of-the-art double hoisting algorithm [10] and its mapping onto Osiris in Section V.

Convolutions as Matrix-Vector Products: In Osiris we convert convolutions to their equivalent matrix-vector form to benefit from hoisting in all network layers. This is done by adopting the methods from Orion [23] and specifically employing their Hybrid++ method. We refer interested readers to the paper for the details of the packing strategies.

IV. KERNEL ACCELERATOR UNITS

In this section, we introduce the hardware components, referred to as units, that comprise Osiris. We begin by establishing a consistent notation for polynomials to help contrast our design with prior work. Then, we discuss our choice to use a pipelined FFT architecture, NTT adaptations, and its implementation in Osiris. Next, we show how BConv can be accelerated with a monolithic 2D systolic array. Finally, we discuss how Osiris performs automorphisms and pointwise arithmetic.

A. A Running Example

Consider a polynomial with ring degree $N = 16$ and multiplicative level $\ell = 3$ (four limbs). This polynomial can be represented as a 4×16 matrix, and Figure 2 illustrates this matrix representation. Each element is denoted by i_o . The index i represents the position of the coefficient within its limb (not the coefficient itself). In Figure 2, the polynomial is shown in *natural* order, with indices monotonically increasing from left to right. The same polynomial can also be represented in *bit-reversed* order, which can be distinguished by visualizing only its reordered indices. The subscript, o , indicates the order that coefficients enter or leave a hardware component. For example, the element highlighted in red in Figure 2 conveys that the first coefficient of the first limb is in the initial set of four values to enter or leave a unit per cycle.

As we introduce each of Osiris' hardware units in the following subsections, we will refer back to this example to concretize the concepts. The order coefficients enter and leave functional units in Osiris is different from prior FHE accelerators. A key insight is that interleaving the computations of distinct limbs enables the lockstep execution of larger FHE kernels such as ModChange. Therefore, explicitly writing each

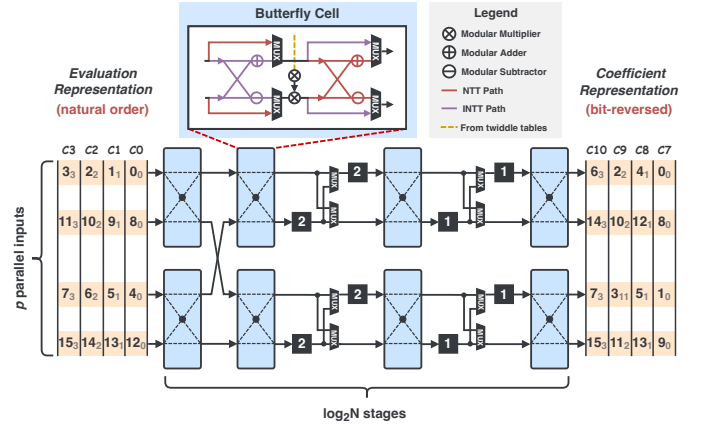


Fig. 3: A 4-parallel MDC unit (numbered boxes indicate buffer length) performing an INTT on the first limb of the example polynomial. The *same* input ordering shown above is compactly described by the i_o notation. C0 denotes cycle 0.

coefficient in a polynomial as i_o allows us to better compare this new dataflow with prior work.

B. Accelerating I/NTT

The Multi-Delay Commutator: The Multi-Delay Commutator (MDC) belongs to a family of pipelined FFT architectures [26], [33], [50]. In Osiris we employ a radix-2 pipelined MDC architecture to accelerate the (inverse) number theoretic transform (I/NTT). Two parameters define each MDC unit: s , the number of stages in the design, settings its depth, and p , the number of parallel inputs and outputs to each stage, defining its width. Radix-2 pipelined architectures perform the Cooley-Tukey FFT algorithm [17], which has $\log_2(N)$ stages with $N/2$ butterfly operations in each stage. By design, each MDC stage performs *all* the butterfly operations of the corresponding Cooley-Tukey stage. Therefore, any radix-2 design will have $s = \log_2(N)$ stages. A p -parallel MDC design consists of $p/2$ butterfly *cells* per stage, each computing a single two input butterfly per cycle. In Cooley-Tukey, the difference in coefficient indices between inputs varies from stage to stage. The MDC supports this by using a series of fixed buffers and multiplexers placed between each stage to *commute* the order of inputs. In total, each MDC has $N - p$ buffers. We classify the MDC architecture as *systolic-esque* since all butterfly cells operate in lockstep to propagate data through the unit in a pipelined manner with minimal control logic.

Adapting for Osiris: Osiris supports a maximum ring degree of $N = 2^{16}$. Therefore, we set $s = 16^\dagger$. We set the width of each MDC to be $p = 512$ after carefully evaluating the bandwidth characteristics of BSGS hoisting (see Section V). Figure 3 visualizes a small 4-parallel MDC architecture performing INTT on the first limb of the example polynomial introduced in Figure 2 and highlights three key aspects of the design. First, each butterfly cell contains *two* modular multipliers, one for on-the-fly twiddle factor generation (OF-Twiddle) [39] and another for the butterfly operation itself.

[†]For any $N' < 2^{16}$, we skip the first $16 - \log_2(N')$ stages in the design.

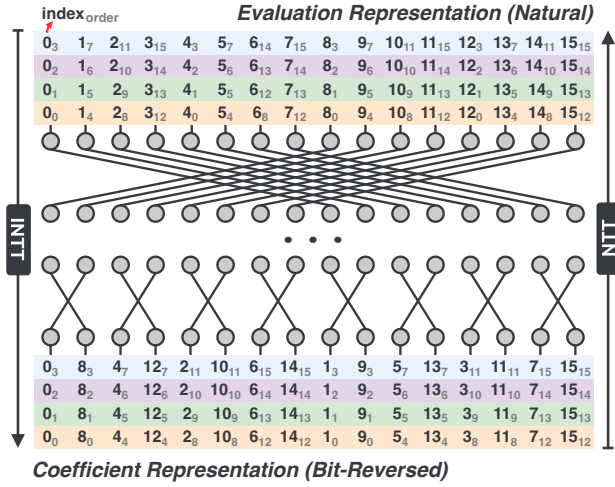


Fig. 4: Visualizing the interleaved input and output order of the 4-parallel MDC unit introduced in Figure 3 using i_o notation introduced in Section IV-A.

OF-Twiddle decomposes N unique twiddle factors into two tables of size \sqrt{N} , enabling the generation of any twiddle factor by multiplying two entries, one from each table. This decomposition reduces the storage requirement of twiddle factors from 13 MB to just 0.20 MB, with groups of $p = 16$ lanes sharing a common set of twiddle tables. Second, pipelined FFT architectures are bi-directional: data flowing in one direction computes the FFT, while the other direction performs the inverse FFT. Figure 3 illustrates this concept, with the highlighted butterfly cell featuring both INTT and NTT paths. For clarity, we omit drawing the additional control logic between stages that routes both directions [43]. In Section V, we show how the bi-directional nature of pipelined NTT architectures can double the throughput of the DiagMult kernel. Third, MDC architectures always accept and produce p elements per cycle. In the following subsection, we detail how this constant flow of data simplifies rate-matching.

Interleaving I/NTTs: We choose the MDC design for its inherent ability *interleave* the processing of independent limbs. Recall from Algorithm 1 that I/NTT operations occur in the ModChange kernel as part of the $\text{INTT} \rightarrow \text{BConv} \rightarrow \text{NTT}$ routine. Each I/NTT acts on unique *rows* (limbs) of the matrix representation. In contrast, BConv is fundamentally a matrix multiplication. Rows of a base table are multiplied with *columns* of an input polynomial. Each column in this polynomial contains coefficients from *all* its limbs. Therefore, performing INTTs on each limb sequentially stalls the ModChange pipeline until all limbs have been processed.

In Osiris, we avoid these stalls by forcing the output order of the MDC INTT to match the column-wise input order required by BConv. Figure 4 visualizes this new *interleaved* I/NTT format using the i_o notation from Section IV-A and the smaller 4-parallel MDC introduced in Figure 3. Note that while the INTT input indices are identical to those in Figure 2, the subscripts are different. Specifically, we begin by feeding $p = 4$ values from the first limb to our example MDC INTT

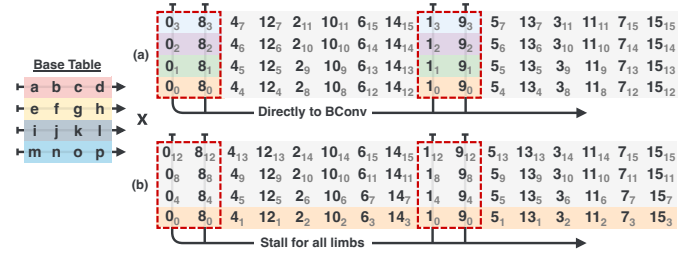


Fig. 5: BConv input ordering in (a) Osiris and (b) prior FHE accelerators using the same example polynomial introduced in Section IV-A. Highlighted elements indicate coefficients available after four cycles. Note that in Osiris, we can begin the BConv operation immediately since *rows* of a base table are multiplied with *columns* of the input polynomial.

unit. In the next cycle, rather than the next four values from the first limb, we instead feed the first four values from the second limb, beginning a second INTT. We continue this interleaving process for all limbs in the polynomial before returning to the first limb for its second set of four values. As a result, coefficients flow from the MDC INTT in the column-wise order required by BConv, allowing the two units to operate together in lockstep.

Differences from Prior Work: Figure 5 captures the differences in INTT output (BConv input) ordering between Osiris and prior FHE accelerators. Note that the BConv operation in Osiris can begin well before any single INTT completes. To support interleaving, we simply by extend the buffers between each MDC stage by a factor equal to the number of interleaved limbs, compensating for the increased delay between butterflies of the same I/NTT. Therefore the 512-parallel MDC units on Osiris have 13 MB of buffers.

C. Accelerating BConv

2D Systolic Arrays: The core operation of BConv is a large matrix-matrix multiplication, and it is natural to consider accelerating it with a 2D systolic array. Each cell performs one multiply-accumulate (MAC) operation per cycle, contributing to a partial sum that is passed down to neighboring PEs. Outputs stream from cells at the periphery of the array. When the array's dimensions are smaller than the dimensions of the input matrices, blocked matrix multiplications are required.

Adapting for Osiris: In Osiris, we accelerate BConv with a monolithic 2D input-stationary systolic array. The height of our array is determined by the largest height (number of limbs) of any input polynomial passed to BConv. In hybrid key-switching, all BConv operations act on input polynomials of at most α limbs, either as the size of each decomposed digit in ModUp or as the number of limbs in the auxiliary modulus, P , in ModDown (see Table I). We set the maximum supported $\alpha = 16$ in order to minimize the size of key-switching keys while remaining 128-bit secure. Therefore, we also size the height of the systolic array to be 16 cells tall. Likewise, we size the BConv array to be 512 cells wide to seamlessly accept the MDC's output of $p = 512$ coefficients per cycle. As a

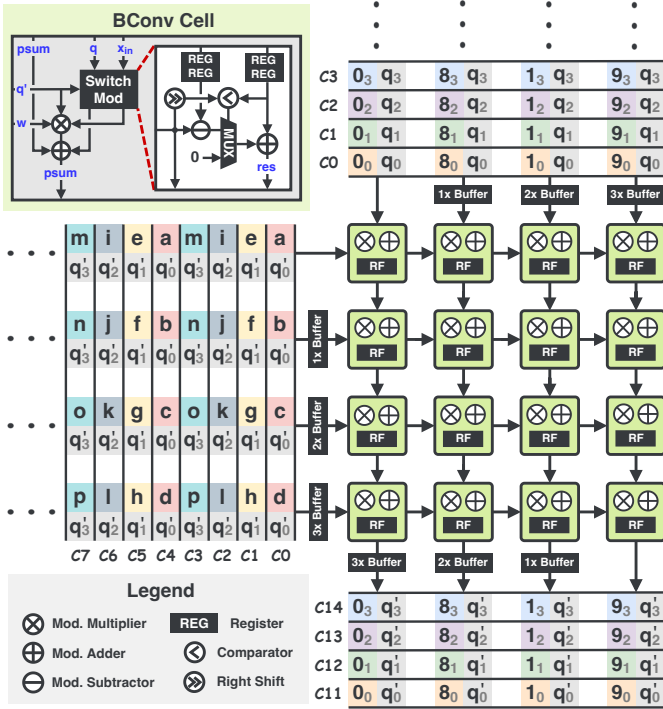


Fig. 6: A 4×4 BConv array converting $\ell = 3$ interleaved input limbs (mod Q) into $\ell = 3$ interleaved output limbs (mod Q'). The first row of PEs each contain an additional modular multiplier for the preliminary limb-wise scaling in BConv. For clarity, only the psum output is shown.

result, the MDC naturally partitions the larger $\alpha \times N$ input polynomial into smaller blocks, each of size $\alpha \times p$, that are then fed directly to the systolic array.

Figure 6 illustrates a smaller 4×4 BConv systolic array processing the interleaved polynomial introduced in Figure 4, with $N = 16$ and $\ell = 3$. For consistency, we use the same base table as in Figure 5, converting a input polynomial from modulus $Q = \prod_{i \leq 3} q_i$ to a new modulus $Q' = \prod_{i \leq 3} q'_i$. We highlight four features in Figure 6. First, interleaved coefficients (*top*) and base table constants (*left*) are first skewed by buffers of differing lengths before entering the array. Skewed input matrices are common in 2D systolic arrays and ensure that the correct partial sums (*psums*) are accumulated within the array. Second, input polynomial coefficients are double-buffered. We reserve two registers within each PE for input coefficients: one for the coefficient from the current $\alpha \times p$ (4×4 in Figure 6) block being processed, and another for preloading coefficients from the next block. Third, all PEs perform the same *switch-modulus multiply-accumulate* (SMAC) operation. For a base table constant w , an input coefficient x_{in} , and an old (new) modulus q (q'), we define this operation as:

$$psum \leftarrow psum + w \cdot \text{SwitchModulus}_{q \rightarrow q'}(x_{in}) \pmod{q'}$$

Since the SwitchModulus function involves both the old modulus, q , and the new modulus, q' , we stream each q'_i alongside its corresponding row of base table constants. This ensures that all partial sums are accumulated under the same

new modulus. Finally, output coefficients leave the array in an interleaved fashion and are unskewed by a set of complementary buffers. Since BConv is part of the larger ModChange pipeline, keeping coefficients interleaved ensures that they can be passed directly to subsequent MDC NTT hardware.

Differences from Prior Work: Notably, ARK [38] and SHARP [37] employ systolic arrays to accelerate BConv. Since these designs do not interleave limbs, the memory access patterns require many smaller arrays be used. The authors allocate 1024 1×6 (ARK) or 2×8 (SHARP) output-stationary systolic arrays, one per lane. Unique base table constants are then broadcasted across the 256 lanes in each cluster using central broadcast units (BrUs). In contrast, the interleaved ordering in Osiris enables base table constants to be passed systolically between cells in a single 2D array.

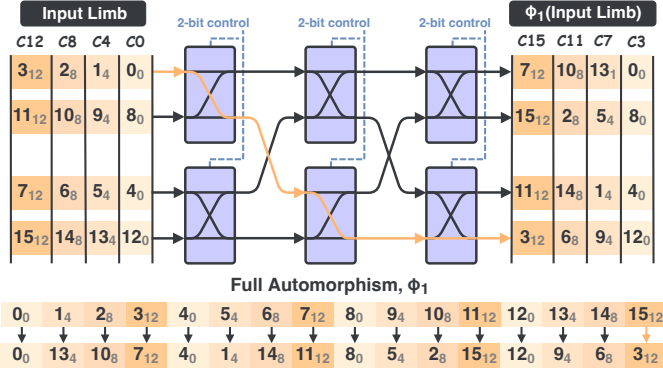
D. Automorphisms

We now describe how Osiris efficiently performs automorphisms. The automorphism applies the index permutation $\phi_r : i \rightarrow i \cdot 5^r \pmod{N}$ to each limb of a polynomial in the evaluation representation and in natural order. This permutation cyclically shifts values in the underlying vector message by r slots to the left. ARK [38] notes that with ring degree $N = 2^{16}$, the automorphism can be decomposed into 2^8 smaller permutations of 2^8 indices. More generally, we can build any automorphism from permutations to subsets of coefficients if each subset, S , satisfies two conditions: $|S|$ is a power of two, and the indices in S are evenly spaced by $\frac{N}{|S|}$. When $|S| = N$, we recover the original automorphism. This is fortuitous to Osiris as the MDC unit produces $p = 512$ evenly spaced elements per cycle in natural order. Therefore, when an automorphism is required, the MDC's output can be directly passed to any p -to- p permutation network, completing the operation over N/p cycles. In Osiris, we choose to perform these permutations with a 512-to-512 Beneš network [8].

Figure 7 visualizes a smaller 4-to-4 Beneš network performing ϕ_1 on the first limb of an interleaved polynomial in natural order with $N = 16$ and $\ell = 3$. We highlight three features of Figure 7. First, since input limbs are interleaved, elements from the same limb enter the network once every $\ell + 1 = 4$ cycles. Second, subsets of $p = 4$ indices, evenly spaced by $N/p = 4$, enter the Beneš network per cycle. Since each subset meets the criteria above, any automorphism can be decomposed into local permutations of these subsets. Third, ϕ_1 permutes each element *from* index i *to* index $i \cdot 5^1 \pmod{16}$. We highlight the path that maps index 3 to index $3 \cdot 5^1 \pmod{16} = 15$, alongside the full ϕ_1 automorphism.

E. Hadamard Unit and Key Generation

Osiris also includes a unit responsible for all point-wise multiplications and additions present in CKKS. This Hadamard unit consists of $p = 512$ 1D systolic arrays, each of height d_{num} , which help to efficiently perform inner products with key-switching keys. Each cell contains four modular multipliers and adders to support both KeyMult and diagonal multiplication simultaneously, which prevents stalling in our



difference is motivated by our choice to feed limbs through Osiris in an *interleaved* fashion. Recall from Section IV that interleaving resolves the differences between the desired input order of I/NTT and BConv and enables the units to operate together in lockstep. Therefore, when mapped onto Osiris, it is useful to view the ModChange operation as a single, macro-pipeline with a throughput of one output limb every N/p cycles.

We also note that while the BSGS algorithm reduces the number of ciphertext rotations in matrix-vector products, it does not reduce the number of plaintext diagonal multiplications. When the number of non-zero diagonals is large, a significant fraction of end-to-end latency comes from OF-Limb. To mitigate this bottleneck, we leverage the bidirectional nature of pipelined NTT architectures to reverse the direction of our ModChange’s MDC INTT unit for the duration of OF-Limb. Since OF-Limb generates diagonals through repeated NTTs, the INTT unit would otherwise be left idle. This strategy doubles the throughput of OF-Limb, and we place Hadamard units on each side of Osiris to generate and accumulate partial products.

VI. METHODOLOGY

CPU Setup: Alongside Osiris, we evaluate our benchmarks on an h3-standard-88 GCP instance with a Intel Xeon Platinum 8481C processor clocked at 2.7 GHz and 352 GB of RAM. We use Lattigo v5.2 to generate and evaluate our benchmarks.

Incorporating Prior Work: We support a maximum bit-width of 40 bits and therefore adopt the same double-prime scaling techniques as SHARP [37] to maintain high precision bootstrapping. The choice of 40 bits over SHARP’s 36 bits allows traditional single-prime scaling techniques to be used in the lowest level matrix-vector products in bootstrapping. We also adopt a recent algorithmic optimization from MAD [3] to fuse the ModDown and Rescale stages within each HMult. Its impact on performance is shown in Section VII-C.

Modeling: Given the predictability of performance in the systolic and systolic-inspired units used by Osiris, we developed an analytical performance model. First, we tested the systolic design of each kernel with functional simulation to verify correctness. We then outputted kernel traces from Lattigo running neural inferences to appropriately model the order of operations. Kernels are mapped to corresponding units and timings for each used to estimate total runtime.

Our goal in estimating power and area is to be commensurate with prior work. To do this, we normalize estimates to 7nm. First, we use results from SHARP [37] to scale the 64-bit Montgomery multiplier units from BTS [40] to 40 bits for an area (power) of $1236 \mu\text{m}^2$ (0.53 mW). The remaining components were synthesized using a commercial 28nm library available to us and scaled to 7nm using scaling factors of 3.6 for area and 3.3 for power, as assumed in prior work [20], [45], [60]. We model power using Synopsys Design Compiler Version T-2022.03-SP2 [59] and assume the worst case switching to conservatively model the distribution of data in cryptographic workloads. Estimates of other logic (e.g., the Beneš network, registers, MUXs, etc.) were synthesized

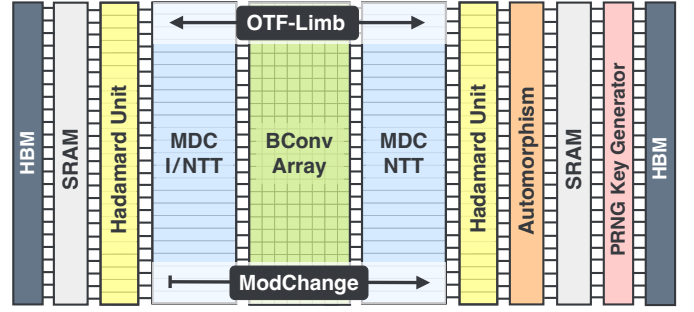


Fig. 9: The complete Osiris architecture. Arrows indicate the flow of data through each kernel unit.

each using the library and scaling down as reported above. Our average SRAM density is $0.45 \text{ mm}^2/\text{MB}$, which is the same as SHARP’s [37]. We have a total SRAM size of 184 MB for keys, partials, decomposed polynomials, and twiddle factors; an additional 26 MB of space is needed for MDC buffering. Finally, we assume the same wire overhead assumption as in ARK [38], adding an additional 10% area to the total design. We clock the chip at 1 GHz.

Benchmarks: We evaluate Osiris on the following benchmarks: **MLP** is a three-layer fully-connected network from SecureML [46] for MNIST. **LoLA** is a three-layer CNN with unencrypted weights from LoLA-CryptoNets [13] also targeting MNIST and used in CraterLake [54]. **LeNet** is a four-layer CNN for MNIST (two strided convolution and two fully connected layers) adopted from Orion [23] and the CHET [22] and EVA [21] FHE compilers. **Bootstrap:** We evaluate the state-of-the-art fully-packed bootstrapping algorithm from Bossuat et al. [10]. **ResNet-20:** We re-implement prior work of Lee et al. [42], replacing convolutions with their analogous matrix-vector products, leaving all else unchanged, including the use of high-degree composite polynomial approximations to ReLU. By also leveraging BSGS, we reduce the number of ciphertext rotations from convolutions by $1.87\times$ over Lee et al. [42]. **HELR-1024** [29] trains an encrypted binary classifier on a subset of MNIST images of size 14×14 . Each epoch performs a forward and backward pass on one mini-batch of size 1024. Latency is reported as the average runtime per epoch. **Sorting** performs bitonic sorting [31] on 2^{14} elements in the range $(0, 1)$. Each comparison is made by compositing twelve 7-degree polynomials. We note that sparsely-packed bootstrapping (when fewer than $N/2$ slots are filled with data) is performed in sorting, HELR-1024, and ResNet-20, which is consistent with prior work.

We adopt the amortized mult time per slot metric ($T_{\text{mult}, a/s.}$) [34] and propose a similar metric that we call the *amortized matrix-vector mult time per slot* defined in Equation (1) for a matrix with d non-zero diagonals. This metric is similar to $T_{\text{mult}, a/s.}$, however aligns more closely with order of operations found in private neural inference.

$$T_{\text{M} \times \text{v} : \#d, a/\text{slot}} = \frac{T_{\text{boot}} + \sum_{\ell=0}^{L-L_{\text{boot}}} T_{\text{M} \times \text{v} : \#d(\ell)}}{L - L_{\text{boot}}} \cdot \frac{2}{N} \quad (1)$$

TABLE II: Residual parameter sets ($\ell \leq L_{\text{eff}}$) used to evaluate Osiris. Moduli (q_i , p_i) and scales (Δ) are in bits. h denotes the Hamming weight of each parameter set’s secret key.

Set	N	n	L_{eff}	α	dnum	q_0	Δ/q_i	p_i	h
I	2^{14}	2^{14}	5	2	3	40	32	40	192
II	2^{14}	2^{14}	7	4	2	40	32	40	192
III [†]	2^{16}	2^{15}	8	5	2	48	36	40	1024
IV [†]	2^{16}	2^{15}	9	5	2	48	36	40	1024

[†]We apply double-prime scaling to the default bootstrapping parameters in Lattigo v5.2 [1], and separately set $\alpha = 14$. We further set $h = 1024$ for 128-bit security as $\log QP_{\text{max}} = 1630$; q_0 is split into two primes.

VII. EVALUATION

In this section, we evaluate Osiris on the aforementioned benchmarks and discuss the benefits afforded by systolic architectures in FHE. We begin by quantifying the implications of hoisting in hardware acceleration. Then we compare Osiris against prior work. Next, we perform a sensitivity study and demonstrate how Osiris’ balanced design enables near linear scaling trends with compute and bandwidth. We close with a roofline analysis [62] to show the effects of hoisting and neural network architecture on utilization.

A. Benchmark Analysis

Table III reports the latency of each benchmark using the parameter sets from Table II on Osiris and with non-hoisted (NH), single-hoisted (SH), and double-hoisted (DH) BSGS matrix \times vector algorithms. Table III also presents Osiris’ improvements over the corresponding CPU implementations.

We highlight two observations in Table III. First, hoisting provides noticeable performance improvements despite lower arithmetic intensity. However, the benefits of hoisting are more pronounced at higher bandwidths. For example, double hoisting reduces the total modular multiplications in fully-packed bootstrapping on Osiris by $1.68\times$ compared to BSGS without hoisting. However, at 1 TB/s, we observe only a $1.09\times$ improvement in latency. This discrepancy arises because we are unable to mask the latency of loading baby-step rotation keys on-chip with the computations of on-the-fly limb extension in double hoisting. As such, the design stalls for 13.9% of its total execution time. Conversely, BSGS without hoisting is mostly compute-limited; significantly less performance gains are achieved at higher bandwidths.

At 2 TB/s, the stalls in double hoisting are reduced to just 0.05 ms, leading to a $1.47\times$ improvement over BSGS without hoisting and approaching the theoretical limit. This promising given the advent of HBM3 [32] and NVIDIA H100 GPUs [49] now boasting an aggregate 8 TB/s of bandwidth. We report latencies at 1 TB/s to be commensurable with prior work [37], [38], [54], however we feel it is now important to consider bandwidths beyond 1 TB/s in FHE accelerators given the pace of bandwidth scaling. We further explore scaling bandwidth and compute in Section VII-C.

Second, we report speedup ranging from $4349\times$ to $20150\times$ at 1 TB/s, with benchmarks that require bootstrapping seeing

TABLE III: Benchmark latencies using non-hoisted (NH), single-hoisted (SH), and double-hoisted (DH) BSGS.

Benchmark	Set	NH	SH	DH	CPU	Improv.
$T_{\text{mult}, \text{a/s.}} (ns)$	III	10.5	9.89	9.58	$68\mu s$	$\times 6433$
$T_{\text{Mv}: 128, \text{a/s.}} (ns)$	III	18.9	17.3	17.4	$112\mu s$	$\times 6438$
MLP (μs)	I	124	125	130	0.57s	$\times 4587$
LoLA (μs)	I	95.5	96.7	97.9	0.47s	$\times 4931$
LeNet (μs)	II	676	663	780	2.94s	$\times 4349$
Bootstrap (ms)	III	3.00	2.82	2.70	17.3s	$\times 6417$
HELR-1024 (ms)	III	2.67	2.61	2.46	15.9s	$\times 6290$
ResNet-20 (ms)	IV	101	96.3	92.4	620s	$\times 7189$
Sorting (s)	IV	1.26	1.20	1.14	23.0K	$\times 20.2K$

(a) All benchmarks evaluated at 1 TB/s, $p = 512$.

Bootstrap (ms)	III	2.77	2.59	1.89	17.3s	$\times 9153$
HELR-1024 (ms)	III	2.49	2.38	2.10	15.9s	$\times 7571$
ResNet-20 (ms)	IV	94.7	89.9	68.5	620s	$\times 9051$
Sorting (s)	IV	1.20	1.13	0.84	23.0K	$\times 27.4K$

(b) Intensive benchmarks also evaluated at 2 TB/s, $p = 512$.

the largest improvement. The higher multiplicative levels in bootstrapping entail significantly more work than operations at lower levels. Osiris (and systolic architectures in general) are well-suited for kernels with large, consistent streams of data. The matrix-vector products present in bootstrapping embody this as they contain many sequential BConv and I/NTT operations. At the same time, the increased arithmetic intensity provided by on-the-fly limb extension is greatest when ℓ is large, as more plaintext diagonals must be generated. Therefore, while Osiris performs well across a spectrum of workloads, it excels in the most computationally-intense scenarios. The growing complexity of FHE applications is a promising trend for Osiris.

B. Comparisons with Prior Work

Latency: We now compare Osiris’ performance against the prior work of BTS [40], CraterLake [54], ARK [38], and SHARP [37]. Figure 10 focuses on the latency of bootstrapping and ResNet-20 inference, since these two benchmarks are common across all designs. To account for differences in parameter sets, we normalize Bootstrap latency by L_{eff} .

We highlight two features of Figure 10. First, Osiris achieves state-of-the-art on both benchmarks at a bandwidth of 1 TB/s. We also expect to see better performance scaling with bandwidth than SHARP [37], where an alternative minimum key-switching strategy [38] (incompatible with hoisting) is used to boost arithmetic intensity. For instance, ARK [38], using the same technique, reports only a $1.07\times$ improvement on ResNet-20 at 2 TB/s, whereas Osiris improves by $1.35\times$.

Second, we normalize latencies relative to BTS [40], which, to the best of our knowledge, is the only compared design that does not adopt the BSGS algorithm. To fairly compare with BTS, we also implement a bootstrapping variant that excludes both BSGS and hoisting. At 1 TB/s, this variant achieves the highest multiplier utilization of 76.4% and a Bootstrap latency

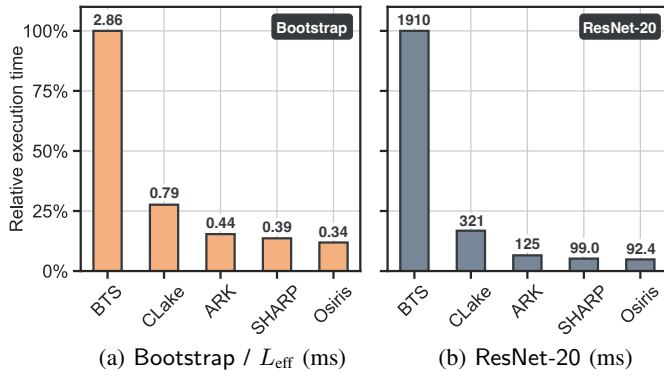


Fig. 10: Comparison of Osiris’ Bootstrap (normalized by L_{eff}) and ResNet-20 performance versus prior work. In Osiris, we set $L_{\text{eff}} = 8$, similar to ARK [38] and SHARP [37]. True latency values are shown above each bar.

TABLE IV: Comparing Osiris’ hardware against prior work. Avg. power reported for ResNet-20 following SHARP [37].

ASIC Design	BW (TB/s)	Bit Width	Mod. Mults.	SRAM (MB)	Area (mm ²)	Power (W)
BTS	1	64	8192	512	373.6	163.2
ARK	1	64	19456	588	418.3	281.3
SHARP	1	36	35776	198	178.8	94.70
CLake [†]	1	28	122K	256	222.7	169.7
Osiris	1	40	32256	210	246.9	116.0

[†]Scaled from 14/12nm to 7nm to match Osiris and [37], [38], [40].

of 5.64 ms, a $4.05\times$ improvement over BTS when normalized by L_{eff} . This demonstrates Osiris’s flexibility in supporting the wide variety of workloads without hoisting. Finally, by adopting the larger 40-bit moduli, rather than SHARP’s 36-bit approach, we improve ResNet-20 performance by 1.2 ms.

Power/area: Table IV compares the hardware in Osiris against prior work. Similar to SHARP [37], we use optimistic 14nm to 7nm area ($2.8\times$) and power ($2.2\times$) scaling factors from [47] to fairly compare against CraterLake [54]. Notably, since modular multiplier area and power scales superlinearly with bit width [37], CraterLake and SHARP can achieve a higher total compute capability for a similar area and power budget. A further component-wise area and power breakdown for ResNet-20 is shown in Table V. Since we allocate *two* MDC I/NTT units in Osiris, the contribution of these units to total area is $2.63\times$ higher than SHARP [37]. In contrast, our BConv hardware consumes just 7.0% (11.3%) of area (power).

C. Sensitivity Study

BSGS Exploration: In Figure 11, we highlight the trade-offs that occur when evaluating matrix-vector products using the double-hoisting BSGS algorithm [10] on Osiris.

In Figure 11a, we split the algorithm into its core kernels and evaluate a matrix-vector product with 64 non-zero diagonals (similar to the matrices found in bootstrapping) for levels $L_{\text{eff}} \leq \ell \leq L$ using Set IV in Table II. In Figure 11b, we focus on just a single matrix-vector product at $\ell = 12$,

TABLE V: Component-wise area (mm²) and power (W) for ResNet-20. MDC buffers are included in I/NTT area/power. Wiring overhead is denoted as WO.

	SRAM	HBM	I/NTT	BConv	Hada.	Auto.	WO.
Area	83.0	29.6	75.8	18.4	14.1	0.56	22.5
Power	19.4	31.8	35.1	14.0	4.34	0.80	10.6

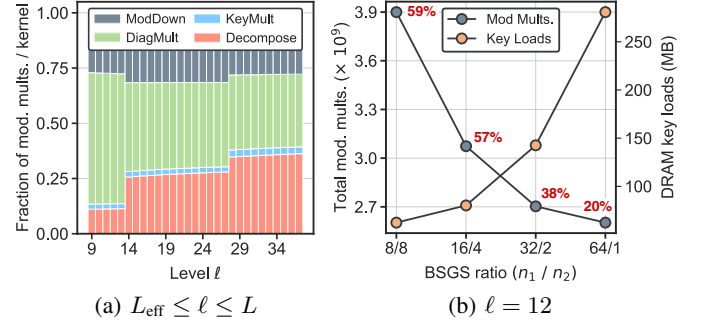


Fig. 11: Exploring the impact of multiplicative level, ℓ , and BSGS ratio on the performance of a double-hoisted matrix-vector product with 64 non-zero diagonals. DiagMult includes OF-Limb. Multiplier utilization (%) is shown in red in (b).

varying the BSGS ratio (n_1/n_2) from 1 to 64 and plotting the number of modular multiplications alongside rotation key loads from DRAM. Recall from Section V that a goal of the GSC dataflow is to mask the latency of loading each baby-step rotation key by generating n_2 matrix diagonals with OF-Limb. When the number of giant steps, n_2 , is sufficiently large, enough diagonals can be generated to ensure that all loads are masked. For instance, in Figure 11b, a BSGS ratio of 1 avoids stalls entirely and maintains high multiplier utilization at 59%. However, when moving beyond $n_2 = 4$ to $n_2 = 1$, the design stalls for 35% of its execution time, reducing utilization to just 20%. This increases our latency on Osiris by $1.96\times$ despite $1.50\times$ fewer modular multiplications. Thus, while key multiplication contributes only marginally to modular operations (Figure 11a), it is often the deciding factor for the optimal BSGS ratio on Osiris.

Dataflow Optimizations: In Figure 12, we isolate the impacts of accelerator-specific algorithmic optimizations and the effects of scaling compute and bandwidth on ResNet-20 performance. In Figure 12a, we begin with a baseline implementation of Osiris at 1 TB/s with neither the GSC dataflow nor limb interleaving and build to a design that incorporates both alongside ModDown fusing. By adopting the GSC dataflow for ResNet-20, we reduce stalls from loading rotation keys by 113 ms (56 ms). Limb interleaving further boosts PE utilization from 8% (14%) by preventing additional stalls between our I/NTT and BConv hardware in each ModChange operation. ModDown fusing further reduces ResNet-20 runtime by 7% (8%).

We also note that ResNet-20 latency roughly halves as we double both memory bandwidth and compute. The near linear scaling trends seen here are deliberate and follow naturally from scaling Osiris’s array width. This highlights how the

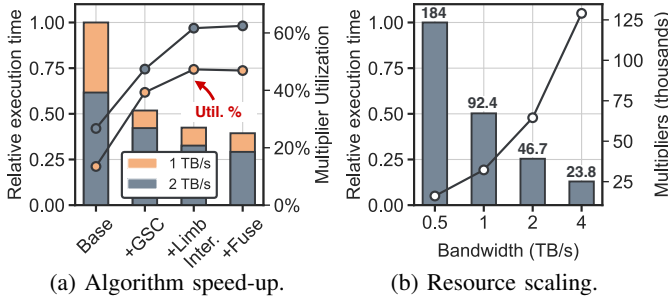


Fig. 12: Quantifying the impact of algorithmic optimizations and bandwidth scaling on Osiris' ResNet-20 latency.

simple, lockstep execution a systolic architecture can target a variety of applications and environments with ease.

Roofline Plots: In Figure 13, we use roofline plots to better understand the impact of hoisting and neural network architecture on Osiris' performance. Roofline plots offer an intuitive way to identify sources of performance bottlenecks and inform better algorithm and hardware design. This attribute is particularly valuable in the context of FHE, where upwards of 100 GB of rotation keys may be streamed on-chip per ResNet-20 inference. We define arithmetic intensity here to be the number of modular multiplications per byte of DRAM traffic; this metric has also been adopted by MAD [3]. In Figure 13a, we visualize the characteristics of our seven benchmarks at both 1 TB/s and 2 TB/s. In Figure 13b, we focus specifically on ResNet-20 and sweep its implementation using the matrix-vector algorithms in Section V.

We highlight three features of Figure 13. First, Osiris' multiplier utilization ranges from 46% to 74% and increases with bandwidth. The extent of this increase is correlated with the amount of hoisting performed. Second, arithmetic intensity generally *decreases* with increasing bandwidth. This effect occurs because we independently optimize the ratio of baby-steps to giant-steps, n_1/n_2 , at each bandwidth. At 2 TB/s, the optimal ratios are often *higher*, hoisting out more expensive operations and approaching the results derived in [10]. Third, our hardware is well-balanced and algorithms are situated near the roofline's ridge point. This outcome is due to the deliberate sizing of Osiris' width and speaks to the ease at which we can reason about higher-level concepts with systolic architectures. This balanced design enables the promising scaling trends seen in Figure 12b.

VIII. RELATED WORK

CPU/GPU: Multiple FHE software libraries are now available [1], [7], [16], [27], [55], providing high-performance CPU implementations. The high computational and memory bandwidth of GPUs provide a promising alternative to CPUs for running FHE. A collection of GPU implementations now exist. One of the first to port FHE to GPU was cuHE [19], paving the way for future work such as 100x [34] and Cheddar [36]. Others have fine-tuned specific kernels (e.g., NTT) for GPUs achieving multiple orders of magnitude improvement [51].

FPGAs: Prior [5], [53], [63] employ FPGAs as lower power, more custom alternative to GPUs, and further accelerates

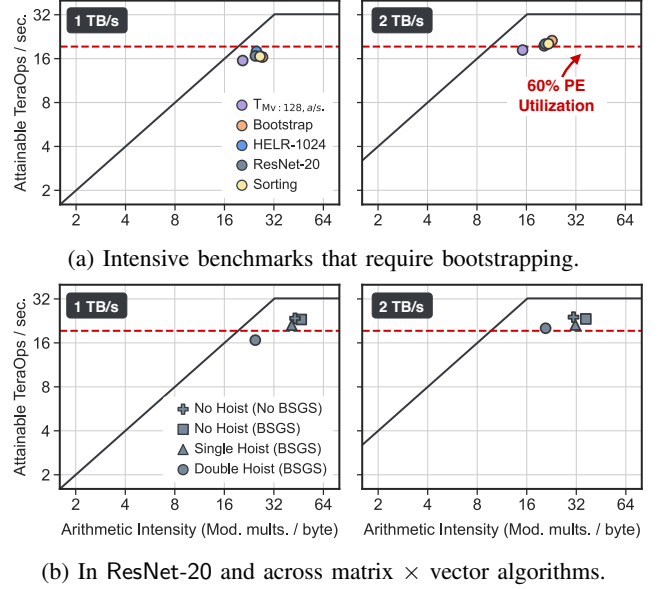


Fig. 13: Roofline analysis of Osiris' neural network benchmarks for varying bandwidths and matrix-vector algorithms.

FHE. Notably, FAB [5] is the first to support CKKS bootstrapping on FPGAs and also employs the double-hoisting optimizations [10]. However, while FPGA-based approaches are significantly more flexible than ASIC designs, they still lack the available on-chip memory to scale compute without bandwidth concerns. The problems above motivate the need for ASIC acceleration. HEAX proposes an architecture for ciphertext-ciphertext multiplication and reports two orders of magnitude of speedup [53].

ASIC Acceleration: F1 [25] and Cheetah [52] were among the first ASIC designs to target homomorphic encryption. Since then, many works such as CraterLake [54], BTS [40], ARK [38], and SHARP [37] have targeted *fully* homomorphic encryption, explicitly supporting bootstrapping. CraterLake [54] was the first to realize sub-second ResNet-20 latencies, and optimizations such as minimum key-switching and on-the-fly limb-extension from ARK and SHARP have further reduced latencies by $3\times$. Moreover, the use of 36-bit moduli in SHARP [37], coupled with PRNG key generation from CraterLake [54], have pushed FHE into the realm of practicality, tackling critical issues such as prohibitively large on-chip memories and low arithmetic intensity.

IX. CONCLUSION

In this paper, we proposed Osiris, a scalable systolic approach to accelerating fully homomorphic encryption. The benefits of systolic architectures are many: simplified hardware, intuitive dataflows, and clear compute-memory trade-offs. To complement Osiris, we also proposed limb interleaving, a new data tiling approach that enables the entire architecture to operate in lockstep. When coupled with our giant-step centric dataflow, Osiris achieves state-of-the-art performance across all standard benchmarks at 1 TB/s of bandwidth, with near linear performance improvements as bandwidth and compute are scaled.

ACKNOWLEDGEMENT

This work was supported in part by Graduate Assistance in Areas of National Need (GAANN). The research was developed with funding from the NSF CAREER award #2340137 and from DARPA, under the Data Protection in Virtual Environments (DPRIVE) program, contract HR0011-21-9-0003. Reagen and Ebel received generous support from the NY State Center for Advanced Technology in Telecommunications (CATT) and a gift award from Google. We also thank Alhad Daftardar for the help in synthesizing our Beneš network. The views, opinions, and/or findings expressed are those of the authors and do not necessarily reflect the views of sponsors.

REFERENCES

- [1] “Lattigo v4,” Online: <https://github.com/tuneinsight/lattigo>, Aug. 2022, ePFL-LDS, Tune Insight SA.
- [2] “DaCapo: Automatic bootstrapping management for efficient fully homomorphic encryption,” in *33rd USENIX Security Symposium (USENIX Security 24)*. Philadelphia, PA: USENIX Association, Aug. 2024. [Online]. Available: <https://www.usenix.org/conference/usenixsecurity24/presentation/cheon>
- [3] R. Agrawal, L. Castro, C. Juvekar, A. Chandrakasan, V. Vaikuntanathan, and A. Joshi, “Mad: Memory-aware design techniques for accelerating fully homomorphic encryption,” in *MICRO*, 2023.
- [4] R. Agrawal, A. Chandrakasan, and A. Joshi, “Heap: A fully homomorphic encryption accelerator with parallelized bootstrapping.”
- [5] R. Agrawal, L. de Castro, G. Yang, C. Juvekar, R. Yazicigil, A. Chandrakasan, V. Vaikuntanathan, and A. Joshi, “Fab: An fpga-based accelerator for bootstrappable fully homomorphic encryption,” 2022.
- [6] E. Aharoni, A. Adir, M. Baruch, N. Drucker, G. Ezov, A. Farkash, L. Greenberg, R. Masalha, G. Moshkovich, D. Murik, H. Shaul, and O. Soceanu, “HeLayers: A tile tensors framework for large neural networks on encrypted data,” *Proceedings on Privacy Enhancing Technologies*, vol. 2023, no. 1, pp. 325–342, jan 2023. [Online]. Available: <https://doi.org/10.56553/2Fpopets-2023-0020>
- [7] A. A. Badawi, J. Bates, F. Bergamaschi, D. B. Cousins, S. Erabelli, N. Genise, S. Halevi, H. Hunt, A. Kim, Y. Lee, Z. Liu, D. Micciancio, I. Quah, Y. Polyakov, S. R.V., K. Rohloff, J. Saylor, D. Saponitsky, M. Triplett, V. Vaikuntanathan, and V. Zucca, “Openfhe: Open-source fully homomorphic encryption library,” *Cryptology ePrint Archive*, Paper 2022/915, 2022, <https://eprint.iacr.org/2022/915>. [Online]. Available: <https://eprint.iacr.org/2022/915>
- [8] V. E. Beneš, “Optimal rearrangeable multistage connecting networks,” *The Bell System Technical Journal*, vol. 43, no. 4, pp. 1641–1656, 1964.
- [9] F. Benhamouda, T. Lepoint, C. Mathieu, and H. Zhou, “Optimization of bootstrapping in circuits,” 2016.
- [10] J.-P. Bossuat, C. Mouchet, J. Troncoso-Pastoriza, and J.-P. Hubaux, “Efficient bootstrapping for approximate homomorphic encryption with non-sparse keys,” *Cryptology ePrint Archive*, Paper 2020/1203, 2020, <https://eprint.iacr.org/2020/1203>. [Online]. Available: <https://eprint.iacr.org/2020/1203>
- [11] Z. Brakerski, C. Gentry, and V. Vaikuntanathan, “(leveled) fully homomorphic encryption without bootstrapping,” *ACM Transactions on Computation Theory (TOCT)*, vol. 6, no. 3, pp. 1–36, 2014.
- [12] Z. Brakerski and V. Vaikuntanathan, “Fully homomorphic encryption from ring-lwe and security for key dependent messages,” in *Annual cryptology conference*. Springer, 2011, pp. 505–524.
- [13] A. Brutzkus, O. Elisha, and R. Gilad-Bachrach, “Low latency privacy preserving inference,” in *International Conference on Machine Learning*, 2019.
- [14] J. H. Cheon, K. Han, A. Kim, M. Kim, and Y. Song, “A full rms variant of approximate homomorphic encryption,” in *Selected Areas in Cryptography–SAC 2018: 25th International Conference, Calgary, AB, Canada, August 15–17, 2018, Revised Selected Papers 25*. Springer, 2019, pp. 347–368.
- [15] J. H. Cheon, A. Kim, M. Kim, and Y. Song, “Homomorphic encryption for arithmetic of approximate numbers,” in *International conference on the theory and application of cryptology and information security*. Springer, 2017, pp. 409–437.
- [16] J. H. Cheon, A. Kim, M. Kim, and Y. Song, “Homomorphic encryption for arithmetic of approximate numbers,” in *Advances in Cryptology – ASIACRYPT 2017*, T. Takagi and T. Peyrin, Eds. Cham: Springer International Publishing, 2017, pp. 409–437.
- [17] J. W. Cooley and J. W. Tukey, “An algorithm for the machine calculation of complex fourier series,” *Mathematics of Computation*, vol. 19, no. 90, pp. 297–301, 1965. [Online]. Available: <http://www.jstor.org/stable/2003354>
- [18] M. Cowan, D. Dangwal, A. Alaghi, C. Trippel, V. T. Lee, and B. Reagen, “Porcupine: A synthesizing compiler for vectorized homomorphic encryption,” in *Proceedings of the 42nd ACM SIGPLAN International Conference on Programming Language Design and Implementation*, ser. PLDI 2021. New York, NY, USA: Association for Computing Machinery, 2021, p. 375–389. [Online]. Available: <https://doi.org/10.1145/3453483.3454050>
- [19] W. Dai, “cuHE: CUDA homomorphic encryption library.” [Online]. Available: <https://github.com/vernamlab/cuHE>
- [20] N. P. Database, “Tsmc 16ff+ (finfet plus),” 2023. [Online]. Available: [https://product.statnano.com/product/6775/16ff-\(finfet-plus\)](https://product.statnano.com/product/6775/16ff-(finfet-plus))
- [21] R. Dathathri, B. Kostova, O. Saarikivi, W. Dai, K. Laine, and M. Musuvathi, “EVA: an encrypted vector arithmetic language and compiler for efficient homomorphic computation,” in *Proceedings of the 41st ACM SIGPLAN Conference on Programming Language Design and Implementation*. ACM, jun 2020. [Online]. Available: <https://doi.org/10.1145%2F3385412.3386023>
- [22] R. Dathathri, O. Saarikivi, H. Chen, K. Laine, K. Lauter, S. Maleki, M. Musuvathi, and T. Mytkowicz, “Chet: An optimizing compiler for fully-homomorphic neural-network inferencing,” in *Proceedings of the 40th ACM SIGPLAN Conference on Programming Language Design and Implementation*, ser. PLDI 2019. New York, NY, USA: Association for Computing Machinery, 2019, p. 142–156. [Online]. Available: <https://doi.org/10.1145/3314221.3314628>
- [23] A. Ebel, K. Garimella, and B. Reagen, “Orion: A fully homomorphic encryption compiler for private deep neural network inference,” 2023.
- [24] J. Fan and F. Vercauteren, “Somewhat practical fully homomorphic encryption,” *Cryptology ePrint Archive*, 2012.
- [25] A. Feldmann, N. Samardzic, A. Krastev, S. Devadas, R. Dreslinski, K. Eldefrawy, N. Genise, C. Peikert, and D. Sanchez, “F1: A fast and programmable accelerator for fully homomorphic encryption (extended version),” 2021.
- [26] M. Garrido, “A survey on pipelined fft hardware architectures,” *Journal of Signal Processing Systems*, vol. 94, no. 11, pp. 1345–1364, 2022.
- [27] S. Halevi and V. Shoup, “Algorithms in helib,” *Cryptology ePrint Archive*, Paper 2014/106, 2014, <https://eprint.iacr.org/2014/106>. [Online]. Available: <https://eprint.iacr.org/2014/106>
- [28] S. Halevi and V. Shoup, “Faster homomorphic linear transformations in helib,” in *Advances in Cryptology – CRYPTO 2018*, H. Shacham and A. Boldyreva, Eds. Cham: Springer International Publishing, 2018, pp. 93–120.
- [29] K. Han, S. Hong, J. H. Cheon, and D. Park, “Efficient logistic regression on large encrypted data,” *Cryptology ePrint Archive*, Paper 2018/662, 2018, <https://eprint.iacr.org/2018/662>. [Online]. Available: <https://eprint.iacr.org/2018/662>
- [30] K. Han and D. Ki, “Better bootstrapping for approximate homomorphic encryption,” in *Cryptographers’ Track at the RSA Conference*. Springer, 2020, pp. 364–390.
- [31] S. Hong, S. Kim, J. Choi, Y. Lee, and J. H. Cheon, “Efficient sorting of homomorphic encrypted data with k-way sorting network,” *IEEE Transactions on Information Forensics and Security*, vol. 16, pp. 4389–4404, 2021.
- [32] JEDEC 2023, “High Bandwidth Memory DRAM (HBM3),” JEDEC Solid State Technology Association, Technical Report JESD238A, 2023. [Online]. Available: <https://www.jedec.org/standards-documents/docs/jesd238a>
- [33] J. Johnston, “Parallel pipeline fast fourier transformer,” pp. 564–572(8), October 1983. [Online]. Available: <https://digital-library.theiet.org/content/journals/10.1049/ip-f-1.1983.0088>
- [34] W. Jung, S. Kim, J. H. Ahn, J. H. Cheon, and Y. Lee, “Over 100x faster bootstrapping in fully homomorphic encryption through memory-centric optimization with gpus,” *IACR Transactions on Cryptographic Hardware and Embedded Systems*, vol. 2021, no. 4, p. 114–148, Aug. 2021. [Online]. Available: <https://tches.iacr.org/index.php/TCHES/article/view/9062>

- [35] C. Juvekar, V. Vaikuntanathan, and A. Chandrakasan, "Gazelle: A low latency framework for secure neural network inference," in *Proceedings of the 27th USENIX Conference on Security Symposium*, ser. SEC'18. USA: USENIX Association, 2018, p. 1651–1668.
- [36] J. Kim, W. Choi, and J. H. Ahn, "Cheddar: A swift fully homomorphic encryption library for cuda gpus," 2024. [Online]. Available: <https://arxiv.org/abs/2407.13055>
- [37] J. Kim, S. Kim, J. Choi, J. Park, D. Kim, and J. H. Ahn, "Sharp: A short-word hierarchical accelerator for robust and practical fully homomorphic encryption," in *Proceedings of the 50th Annual International Symposium on Computer Architecture*, ser. ISCA '23. New York, NY, USA: Association for Computing Machinery, 2023. [Online]. Available: <https://doi.org/10.1145/3579371.3589053>
- [38] J. Kim, G. Lee, S. Kim, G. Sohn, M. Rhu, J. Kim, and J. H. Ahn, "ARK: Fully homomorphic encryption accelerator with runtime data generation and inter-operation key reuse," in *2022 55th IEEE/ACM International Symposium on Microarchitecture (MICRO)*. IEEE, oct 2022. [Online]. Available: <https://doi.org/10.1109/52fmicro56248.2022.00086>
- [39] S. Kim, W. Jung, J. Park, and J. H. Ahn, "Accelerating number theoretic transformations for bootstrappable homomorphic encryption on gpus," in *2020 IEEE International Symposium on Workload Characterization (IISWC)*. IEEE, Oct. 2020. [Online]. Available: <http://dx.doi.org/10.1109/IISWC50251.2020.00033>
- [40] S. Kim, J. Kim, M. J. Kim, W. Jung, J. Kim, M. Rhu, and J. H. Ahn, "BTS," in *Proceedings of the 49th Annual International Symposium on Computer Architecture*. ACM, jun 2022. [Online]. Available: <https://doi.org/10.1145/2f3470496.3527415>
- [41] A. Krastev, N. Samardzic, S. Langowski, S. Devadas, and D. Sanchez, "A tensor compiler with automatic data packing for simple and efficient fully homomorphic encryption," *Proc. ACM Program. Lang.*, vol. 8, no. PLDI, jun 2024. [Online]. Available: <https://doi.org/10.1145/3656382>
- [42] E. Lee, J.-W. Lee, J. Lee, Y.-S. Kim, Y. Kim, J.-S. No, and W. Choi, "Low-complexity deep convolutional neural networks on fully homomorphic encryption using multiplexed parallel convolutions," in *Proceedings of the 39th International Conference on Machine Learning*, ser. Proceedings of Machine Learning Research, K. Chaudhuri, S. Jegelka, L. Song, C. Szepesvari, G. Niu, and S. Sabato, Eds., vol. 162. PMLR, 17–23 Jul 2022, pp. 12 403–12 422. [Online]. Available: <https://proceedings.mlr.press/v162/lee22e.html>
- [43] T. Lenart and V. Owall, "Architectures for dynamic data scaling in 2/4/8k pipeline fft cores," *IEEE Transactions on Very Large Scale Integration (VLSI) Systems*, vol. 14, no. 11, pp. 1286–1290, 2006.
- [44] R. Malik, K. Sheth, and M. Kulkarni, "Coyote: A compiler for vectorizing encrypted arithmetic circuits," in *Proceedings of the 28th ACM International Conference on Architectural Support for Programming Languages and Operating Systems, Volume 3*, ser. ASPLOS 2023. New York, NY, USA: Association for Computing Machinery, 2023, p. 118–133. [Online]. Available: <https://doi.org/10.1145/3582016.3582057>
- [45] J. Mo, J. Gopinath, and B. Reagen, "Haac: A hardware-software co-design to accelerate garbled circuits," in *Proceedings of the 50th Annual International Symposium on Computer Architecture*, ser. ISCA '23. ACM, Jun. 2023. [Online]. Available: <http://dx.doi.org/10.1145/3579371.3589045>
- [46] P. Mohassel and Y. Zhang, "Secureml: A system for scalable privacy-preserving machine learning," *Cryptology ePrint Archive*, Paper 2017/396, 2017, <https://eprint.iacr.org/2017/396>. [Online]. Available: <https://eprint.iacr.org/2017/396>
- [47] S. Narasimha, B. Jagannathan, A. Ogino, D. Jaeger, B. Greene, C. Sheraw, K. Zhao, B. Haran, U. Kwon, A. K. M. Mahalingam, B. Kannan, B. Morganfeld, J. Dechene, C. Radens, A. Tessier, A. Hassan, H. Narisetty, I. Ahsan, M. Aminpur, C. An, M. Aquilino, A. Arya, R. Augur, N. Baliga, R. Bhelkar, G. Biery, A. Blaubeurg, N. Borjem-scaia, A. Bryant, L. Cao, V. Chauhan, M. Chen, L. Cheng, J. Choo, C. Christiansen, T. Chu, B. Cohen, R. Coleman, D. Conklin, S. Crown, A. da Silva, D. Dechene, G. Derderian, S. Deshpande, G. Dillway, K. Donegan, M. Eller, Y. Fan, Q. Fang, A. Gassaria, R. Gauthier, S. Ghosh, G. Gifford, T. Gordon, M. Gribelyuk, G. Han, J. Han, K. Han, M. Hasan, J. Higman, J. Holt, L. Hu, L. Huang, C. Huang, T. Hung, Y. Jin, J. Johnson, S. Johnson, V. Joshi, M. Joshi, P. Justison, S. Kalaga, T. Kim, W. Kim, R. Krishnan, B. Krishnan, K. Anil, M. Kumar, J. Lee, R. Lee, J. Lemon, S. Liew, P. Lindo, M. Lingalugari, M. Lipinski, P. Liu, J. Liu, S. Lucarini, W. Ma, E. Maciejewski, S. Madiseti, A. Malinowski, J. Mehta, C. Meng, S. Mitra, C. Montgomery, H. Nayfeh, T. Nigam, G. Northrop, K. Onishi, C. Ordonio, M. Ozbek, R. Pal, S. Parihar, O. Patterson, E. Ramanathan, I. Ramirez, R. Ranjan, J. Sarad, V. Sardesai, S. Soudari, C. Schiller, B. Senapati, C. Serrau, N. Shah, T. Shen, H. Sheng, J. Shepard, Y. Shi, M. Silvestre, D. Singh, Z. Song, J. Sporre, P. Srinivasan, Z. Sun, A. Sutton, R. Sweeney, K. Tabakman, M. Tan, X. Wang, E. Woodard, G. Xu, D. Xu, T. Xuan, Y. Yan, J. Yang, K. Yeap, M. Yu, A. Zainuddin, J. Zeng, K. Zhang, M. Zhao, Y. Zhong, R. Carter, C.-H. Lin, S. Grunow, C. Child, M. Lagus, R. Fox, E. Kaste, G. Gomba, S. Samavedam, P. Agnello, and D. K. Sohn, "A 7nm cmos technology platform for mobile and high performance compute application," in *2017 IEEE International Electron Devices Meeting (IEDM)*, 2017, pp. 29.5.1–29.5.4.
- [48] N. Neda, A. Ebel, B. Reynwar, and B. Reagen, "Ciflow: Dataflow analysis and optimization of key switching for homomorphic encryption," 2023.
- [49] NVIDIA, "NVIDIA H100 Tensor Core GPU," Available: NVIDIA, 2023. [Online]. Available: <https://www.nvidia.com/en-us/data-center/h100/>
- [50] G. O'Leary, "Nonrecursive digital filtering using cascade fast fourier transformers," *IEEE Transactions on Audio and Electroacoustics*, vol. 18, no. 2, pp. 177–183, 1970.
- [51] O. Ozerk, C. Elgezen, A. C. Mert, E. Ozturk, and E. Savas, "Efficient number theoretic transform implementation on gpu for homomorphic encryption," *Cryptology ePrint Archive*, Paper 2021/124, 2021, <https://eprint.iacr.org/2021/124>. [Online]. Available: <https://eprint.iacr.org/2021/124>
- [52] B. Reagen, W. Choi, Y. Ko, V. Lee, G.-Y. Wei, H.-H. S. Lee, and D. Brooks, "Cheetah: Optimizing and accelerating homomorphic encryption for private inference," 2020.
- [53] M. S. Riazi, K. Laine, B. Peltton, and W. Dai, "Heax: An architecture for computing on encrypted data," in *Proceedings of the Twenty-Fifth International Conference on Architectural Support for Programming Languages and Operating Systems*, ser. ASPLOS '20. New York, NY, USA: Association for Computing Machinery, 2020, p. 1295–1309. [Online]. Available: <https://doi.org/10.1145/3373376.3378523>
- [54] N. Samardzic, A. Feldmann, A. Krastev, N. Manohar, N. Genise, S. Devadas, K. Eldefrawy, C. Peikert, and D. Sanchez, "Craterlake: A hardware accelerator for efficient unbounded computation on encrypted data," in *Proceedings of the 49th Annual International Symposium on Computer Architecture*, ser. ISCA '22. New York, NY, USA: Association for Computing Machinery, 2022, p. 173–187. [Online]. Available: <https://doi.org/10.1145/3470496.3527393>
- [55] "Microsoft SEAL (release 4.1)," <https://github.com/Microsoft/SEAL>, Jan. 2023, microsoft Research, Redmond, WA.
- [56] S. Sinha Roy, F. Turan, K. Jarvinen, F. Vercauteren, and I. Verbauwhede, "Fpga-based high-performance parallel architecture for homomorphic computing on encrypted data," in *2019 IEEE International Symposium on High Performance Computer Architecture (HPCA)*, 2019, pp. 387–398.
- [57] N. P. Smart and F. Vercauteren, "Fully homomorphic simd operations," *Des. Codes Cryptography*, vol. 71, no. 1, p. 57–81, apr 2014. [Online]. Available: <https://doi.org/10.1007/s10623-012-9720-4>
- [58] D. Soni, N. Neda, N. Zhang, B. Reynwar, H. Gamil, B. Heyman, M. Nabeel, A. A. Badawi, Y. Polyakov, K. Canida, M. Pedram, M. Maniatakos, D. B. Cousins, F. Franchetti, M. French, A. G. Schmidt, and B. Reagen, "RPU: the ring processing unit," in *IEEE International Symposium on Performance Analysis of Systems and Software, ISPASS 2023, Raleigh, NC, USA, April 23-25, 2023*. IEEE, 2023, pp. 272–282. [Online]. Available: <https://doi.org/10.1109/ISPASS57527.2023.00034>
- [59] Synopsys, "Synopsys synthesis installation notes version t-2022.03 (march 2022)," Mar 2022. [Online]. Available: https://solvet.synopsys.com/Install/installation_guide.jsp?id=212&releasedate=2022-03-07
- [60] TSMC, "16/12nm technology." [Online]. Available: https://www.tsmc.com/english/dedicatedFoundry/technology/logic/l_16_12nm
- [61] A. Viani, P. Jattke, M. Haller, and A. Hithnawi, "Heco: Fully homomorphic encryption compiler," 2023.
- [62] S. Williams, A. Waterman, and D. Patterson, "Roofline: an insightful visual performance model for multicore architectures," *Communications of the ACM*, vol. 52, no. 4, pp. 65–76, 2009.
- [63] Y. Yang, H. Zhang, S. Fan, H. Lu, M. Zhang, and X. Li, "Poseidon: Practical homomorphic encryption accelerator," in *2023 IEEE International Symposium on High-Performance Computer Architecture (HPCA)*, 2023, pp. 870–881.